Journal of Organometallic Chemistry 1038 (2025) 123750

Contents lists available at ScienceDirect

Journal of Organometallic Chemistry

journal homepage: www.elsevier.com/locate/jorganchem

Electron-pump-like near-infrared emissive iridium(III) complexes for hypoxia-tolerant type I & II photodynamic therapy

Zejing Chen [a,c], Qingchao Tu [a], Peiling Dai [c], Yunjian Xu [d], Wenyuan Xu [a], Jingjing Xue [a], Haiyong Ao [a], Xiaoming Hu [a,c,*], Wei Jiang [a,b,*], Shujuan Liu [c], Qiang Zhao [c,*]

[a] Nanchang Key Laboratory for Smart Biomaterials Regulation and Adaptation, School of Materials Science and Engineering, East China Jiaotong University, Nanchang 330013, PR China
[b] Institute of Carbon Neutral New Energy Research, Yuzhang Normal University, Nanchang 330031, PR China
[c] State Key Laboratory of Flexible Electronics (LoFE) & Jiangsu Key, Laboratory of Smart Biomaterials and Theranostic Technology, Institute of Advanced Materials (IAM), Nanjing University of Posts & Telecommunications, Nanjing 210023, PR China
[d] Medical Science and Technology Innovation Center, Institute of Medical Engineering and Interdisciplinary Research, Shandong First Medical University and Shandong Academy of Medical Sciences, Jinan 250000, PR China

ARTICLE INFO

Keywords:
Photodynamic therapy
Hypoxic tumors
Iridium(III) complexes
Type I
reactive oxygen species

ABSTRACT

Photodynamic therapy (PDT) faces challenges in hypoxic tumors due to oxygen-dependent type II mechanisms. Type I PDT, generating oxygen-free radicals, offers a promising alternative but requires efficient photosensitizers. Herein, we report a series of cyclometalated iridium(III) complexes (Ir1, Ir2, Ir3 and Ir4) incorporating electron-rich conjugated CˆN ligands and an electron-deficient NˆN ligand (1,4,5,8-tetraazaphenanthrene, TAP). The synergistic interplay between these ligands enables a pump-like mechanism under photoexcitation, efficiently shuttling electrons to electron-accepting substrates while replenishing electrons from reducing donors, thereby driving robust reactive oxygen free radical generation. These complexes exhibit strong visible-light absorption, near-infrared luminescence with decent quantum efficiency, and effective type I & II PDT activity under hypoxia. In vitro and in vivo studies demonstrate negligible dark toxicity and exceptional phototoxicity upon visible-light irradiation. This work highlights a rational ligand-cooperative design strategy for metal complex-based type I photosensitizers, overcoming hypoxia limitations in conventional PDT while integrating traceable luminescence for potential clinical applications.

1. Introduction

Photodynamic therapy (PDT) as a novel non-invasive therapeutic modality has been applied in clinical treatment for the targeted cancer [1,2], but PDT is still in infancy, with many problems that need to be resolved to release its full potential. For example, tumor are often hypoxic, which leads to a diminished utility of conventional oxygen-dependent PDT [3–5]. To reverse the oxygen imbalance, various self-oxygenation strategies have been established to alleviate the hypoxic tumor microenvironment, such as the delivery of perfluorocarbon- and hemoglobin-based oxygen carriers, the catalytic decomposition of hydrogen peroxide in situ, and the release of reactive oxygen species (ROS) upon other stimulation. However, they often suffer from low oxygen loading, limited prerequisites for oxygen sources in tissues, and forward oxygen release[6]. Fortunately, PDT based on type I mechanism, in which high-toxicity oxygen free radicals rather than singlet oxygen ($^1O_2$) generates has been proved to be low dependent on the oxygen, and is considered to be the most intuitive way to resolve the problem fundamentally[7]. Therefore, the development of high-performance photosensitizers upon type I mechanism is of great significance.

In recent years, a series of type I photosensitizers have been developed by using inorganic nanomaterials such as metal oxides, rare earth materials, and carbon-based materials [8,9]. Nonetheless, these type I photosensitizers based on inorganic materials may present possible safety risks including immune activation, tolerability limits, and chronic toxicological effects[10]. In contrast, organic photosensitizers offer better biocompatibility and biosafety. The most typical representatives

* Corresponding authors at: Nanchang Key Laboratory for Smart Biomaterials Regulation and Adaptation, School of Materials Science and Engineering, East China Jiaotong University, Nanchang 330013, PR China.
E-mail addresses: iamxmhu@ecjtu.edu.cn (X. Hu), jiangwei@yuznu.edu.cn (W. Jiang), iamqzhao@njupt.edu.cn (Q. Zhao).

https://doi.org/10.1016/j.jorganchem.2025.123750
Received 29 May 2025; Received in revised form 11 June 2025; Accepted 17 June 2025
Available online 18 June 2025

are porphyrin derivatives, which occupy almost all the seats of clinically approved photosensitizers currently[11]. Based on such macrocyclic organic compounds, Arnaut and co-workers synthesized a series of bacteriochlorin (tetrahydrogenated porphyrin) photosensitizers that work mainly via type I PDT process[12]. Lindsey and co-workers further found that palladium(II) ion-coordinated bacteriochlorins yielded more efficient type I PDT process than uncoordinated bacteriochlorins[13]. However, these macrocyclic compounds have certain drawbacks including the relatively low-yield synthesis, the inherent rigid and planar aromatic structure that tends to aggregate and result in diminished phototoxicity, and the highly defined tetrapyrrole-based backbone that limits the structural expansion and enhancement of I PDT process to a certain extent[14]. Thus, in despite of Macrocyclic PDT agents, other organic compounds are used for developing the photosensitizers undergoing type I PDT pathway.

As mentioned above, metalation can significantly affect the photochemical processes of organic photosensitizers. Metal complexes are characterized by rich valence states, diverse coordination numbers, and chemical structures and spatial configurations that can be nearly infinitely derived, and are regarded as a great treasure trove for the exploration of type I photosensitizers [15,16]. Among the numerous metal complexes, d-block transition metal complexes including platinum(IV), ruthenium(II), rhodium(III), iridium(III), and osmium(II) complexes have received a lot of attention, mainly because these complexes have modular three-dimensional configurations, which prone to achieve various property modulation such as charge, solubility, and Lewis acidity, metal-ligand bond strength, redox potential, and excited states [17–20]. It is worth mentioning that the type I PDT process is mediated by the triplet excited states of the photosensitizer as same as type II PDT way. For the above metal complexes, the heavy-atom effect could promote spin–orbit coupling, facilitating formation of long-lived triplet excited states and thereby obtaining efficient PDT [21–24]. To date, ruthenium(II) complexes as photosensitizers mainly based on type I process have been widely and intensively studied with some success. However, the luminescent properties of the reported type I ruthenium (II) complex photosensitizers tend to be poor and unfavorable for tracing in vivo and the clinical practice of PDT[25].

In contrast, iridium(III) complexes have superior luminescent properties, as well as better chemical- and photo-stability [26–28], which have been widely used in organic light-emitting diodes, luminescent electrochemical cells, and biosensing and imaging [29–31]. Currently, a mass of phosphorescent iridium(III) complexes with potent phototoxicity have been demonstrated to be the promising PDT agents [32,33]. Most of these studies on iridium(III) complex photosensitizers are related to the common type II processes, and the design guidelines are just limited to how to enhance the $^1O_2$ generation[34], yet the fundamentals about how to promote the type I photoinduced free radicals have not been established. Recently, Brabec and co-workers reported an iridium(III) conjugated to a far-red emitting coumarin with highly favourable properties for PDT even under hypoxic conditions and further clarified that its phototoxicity is mainly derived from superoxide radicals generated by type I photochemical processes[35]. He and workers reported that two benzothiophenylisoquinoline (btiq)-derived iridium(III) complexes could cause photoinduced ferroptosis in tumor cells via a type I mechanism. On the other hand, Elias and co-workers reported a strong photooxidative iridium(III) complex (Ir-TAP), which can directly oxidize biomolecules through photoinduced electron transfer (PeT), achieving the complete destruction of 3D tumor spheroids with internal hypoxia[36]. Huang reported a mitochondria-targeted iridium(III) complex photosensitizer that could photocatalytically oxidizes 1,4-dihydronicotinamide adenine dinucleotide (NADH), generating NAD• radicals via PeT under hypoxia[37]. Nevertheless, the existing few cases provide a realistic basis could not clarify the principles for constructing iridium(III) complex-based photosensitizers with considerable reactive oxygen free radicals. Therefore, developing more iridium(III) complexes with efficient type I process for hypoxic tumor PDT are urgently needed [38–43].

In previous work, we synthesize two kinds of type I photosensitizers by incorporating a coumarin and triphenylamine into cyclometalated and polypyridyl ruthenium(II) complexes, respectively[44]. Both complexes exhibit low oxidation potentials, strong absorptions in the visible region and efficient PDT under hypoxia, but negligible luminescence quantum efficiencies. Herein, we prepared a series of iridium(III) complexes (Ir1, Ir2, Ir3 and Ir4) by selecting four cyclometalating C^N ligands with relatively large conjugated skeleton and harnessing electron-deficient N^N ligand (1,4,5,8-tetraazaphenanthrenem, TAP) which has played important role in modulating photoactive behaviors (Scheme 1). Notably, these iridium(III) complexes show effective type I PDT potency via producing reactive oxygen free radicals effectively, which differ from the reported photooxidants, iridium(III) complex Ir-TAP[45]. Impressively, some of them display high quantum efficiencies in near-infrared region in addition to strong absorptions in the visible region. Further evaluations in vitro and in vivo testified that these four iridium(III) complexes have no toxicity without excitation and good excellent photolethality under the visible light, showing good promise as PDT agents for hypoxic tumor.

2. Experimental section

All reagents and chemicals were procured from commercial sources and used without further purification unless otherwise noted. All solvents were of analytical grade and purified according to standard procedures. The detailed synthesis of complexes and related ligands can be found in Schemes S1-S4. The 1H and ^{13}C NMR spectra of some synthesized compounds in this work were recorded on a Bruker Ultra Shield Plus 400 MHz NMR spectrometer. Deuterated solvents were selected based on the solubility differences of the tested compounds. The molecular weights of larger compounds were determined using a matrix-assisted laser desorption ionization time-of-flight mass spectrometer (MALDI-TOF MS, Voyager DE-STR). The UV–visible absorption spectra of some compounds were measured on a Shimadzu UV–VIS spectrophotometer (UV-2600). The emission spectra of selected compounds were also acquired using the same Shimadzu UV-2600 spectrophotometer. The quantum yields and emission lifetimes of certain compounds were determined using an Edinburgh FLS-920 steady-state and transient spectrometer, with a xenon lamp as the excitation source. Cyclic voltammetry (CV) measurements were performed on a CH620B electrochemical workstation, employing a glassy carbon working electrode, a platinum wire auxiliary electrode, and an Ag/Ag^+ reference electrode, at a scan rate of 0.1 V/s. The electrolyte solution consisted of 0.1 M tetrabutylammonium hexafluorophosphate, which was deoxygenated with nitrogen prior to testing. Time-dependent density functional theory (TD-DFT) calculations were performed using the RB3PW91/SBKJC basis set, and all computations were carried out with the GAMESS software package. Photostability experiments were performed in acetonitrile solution using a xenon lamp (100 mW, 400–800 nm wavelength) for 6 min irradiation. A hypoxic atmosphere containing 1 % O_2 was established using two gas flow controllers (HORIBA STEC, model: SEC-E40) operated in tandem. Specifically, nitrogen gas flow was maintained at 99 times the oxygen flow rate. The two gas streams were combined via a Y-shaped connector to achieve the target hypoxic condition. The details of experimental section were shown in the supplementary data Schemes 1 and 2.

3. Results and discussion

3.1. Design, synthesis and characterization

Previous researches about iridium(III) complexes have revealed that the degree π-conjugation of the cyclometalating ligands impact their lowest singlet and triplet excited state characteristics. As shown in Scheme 1, four iridium(III) complexes (Ir1–Ir4) possess the constant

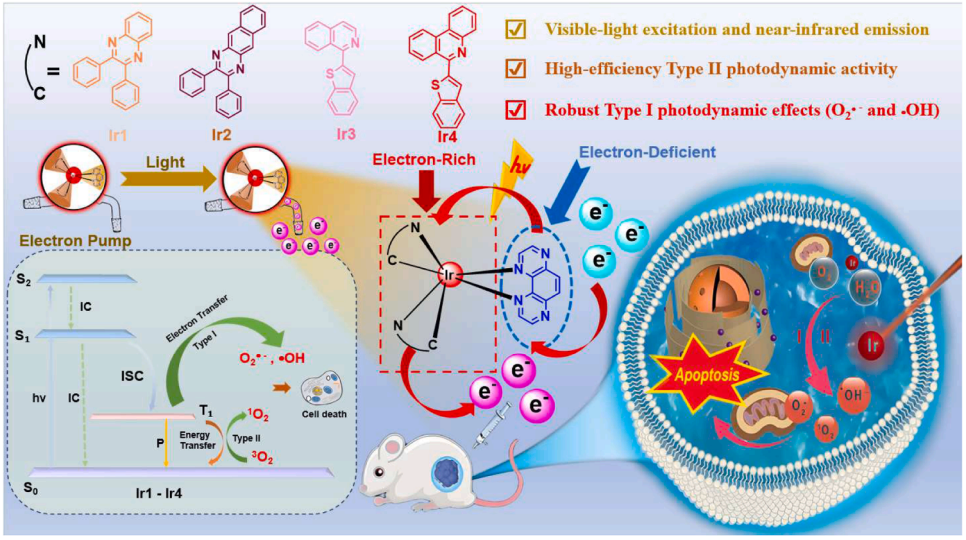

Scheme 1. Chemical structures of iridium(III) complexes and schematic illustration of type I PDT via an electron-pump-like mechanism or type II PDT against hypoxic tumors.

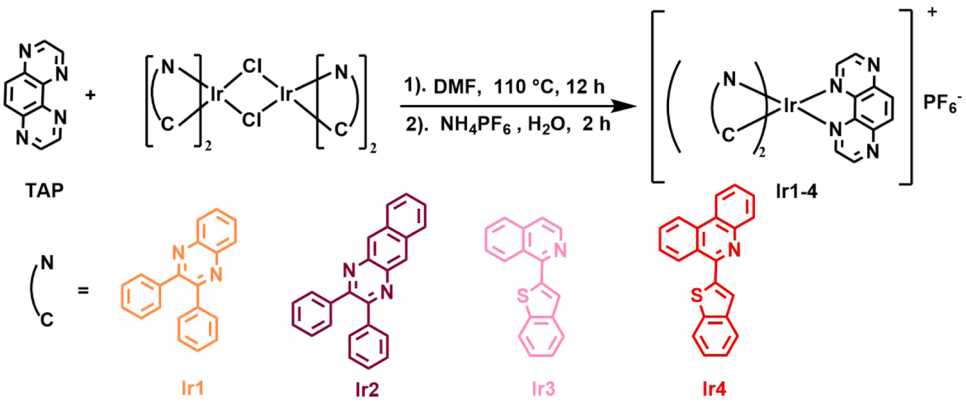

Scheme 2. Synthesis of complexes Ir1–Ir4.

electron-deficient NˆN ligand TAP and diverse cyclometalating CˆN ligands with large π-conjugation degrees (Dpq, Dbq, Bys, Byp) were designed: the NˆN ligands TAP was employed to earn the latent photo-oxidizing power for these complexes, while the CˆN ligands Dpq, Dbq, Bys and Byp are adopted for endowing the desirable long absorption and emission of complexes. It is noted that Dbq or Byp have one more benzene ring within their conjugated system compared with Dpq or Bys, respectively, which facilitates comparative analysis toward the similar complexes. The four CˆN ligands were synthesized by the typical Suzuki-Miyaura cross-coupling reaction with high yields, and the NˆN ligands were synthesized by reported methods. Then the CˆN ligands and $IrCl_3{\cdot}3H_2O$ were added into a mixed solvent of 2-ethoxyethanol and water (v/v = 3/1) and heated at reflux for 12 h to obtain the cyclometalated iridium(III)-chlorobridged dimers, which was precipitated with water and directly used without further purification. Due to the poor solubility of TAP, these iridium(III) complexes were prepared through bridge-splitting reactions of the relative dimers and subsequent complexation with the NˆN coordinating ligand in the dimethyl formamide at 110 °C, which is different from the routine conditions (Scheme 2). Subsequently, the reaction mixture was added to a saturated aqueous solution of ammonium hexafluorophosphate stirred for 2 h and the complexes were obtained by filtration, silica gel column chromatography and recrystallization in n-hexane solution successively. All complexes were characterized by ^1H, ^{13}C nuclear magnetic resonance (NMR) and matrix-assisted laser desorption ionization time-of-flight mass spectrometry (MALDI-TOF-MS) unambiguously, which were presented in detail in the supporting information.

3.2. Photophysical and electrochemical properties

The UV–vis absorption and emission spectra of Ir1–Ir4 at room temperature in acetonitrile are presented in Fig. 1a, and the peaks and extinction coefficients are tabulated in Table 1. All complexes display high-energy absorption bands below about 350 nm with high molar extinction coefficients ($\varepsilon > 2 \times 10^4$ M^{-1} cm^{-1}), which can be assigned to the spin-allowed ligand-centered (LC) π–π* transitions located on both the cyclometalating CˆN and NˆN ligands. The moderately intense absorption bands appeared from 350 to 500 nm are mainly ascribed to the mixture of singlet metal to ligand charge transfer (^{1}MLCT) and singlet ligand to ligand charge transfer (^{1}LLCT), whereas the weaker and lowest-lying absorption bands ($\varepsilon < 1 \times 10^4$ M^{-1} cm^{-1}) at about 500–600 nm are attributed to mixed spin-forbidden transfer ^{3}MLCT and ^{3}LLCT transitions. Remarkably, the absorption bands corresponding to the LC and CT transitions of Ir2 and Ir4 showed significant red shift in comparison to their related model complexes Ir1 and Ir3 due to the larger degree of π-conjugation effect.

Upon optical excitation under ambient conditions, complexes Ir1–Ir4 exhibit prominent near-infrared luminescence with spectral maxima positioned at 658, 783, 682, 709 nm in acetonitrile solutions, respectively, and the phosphorescence characteristics of these complexes are

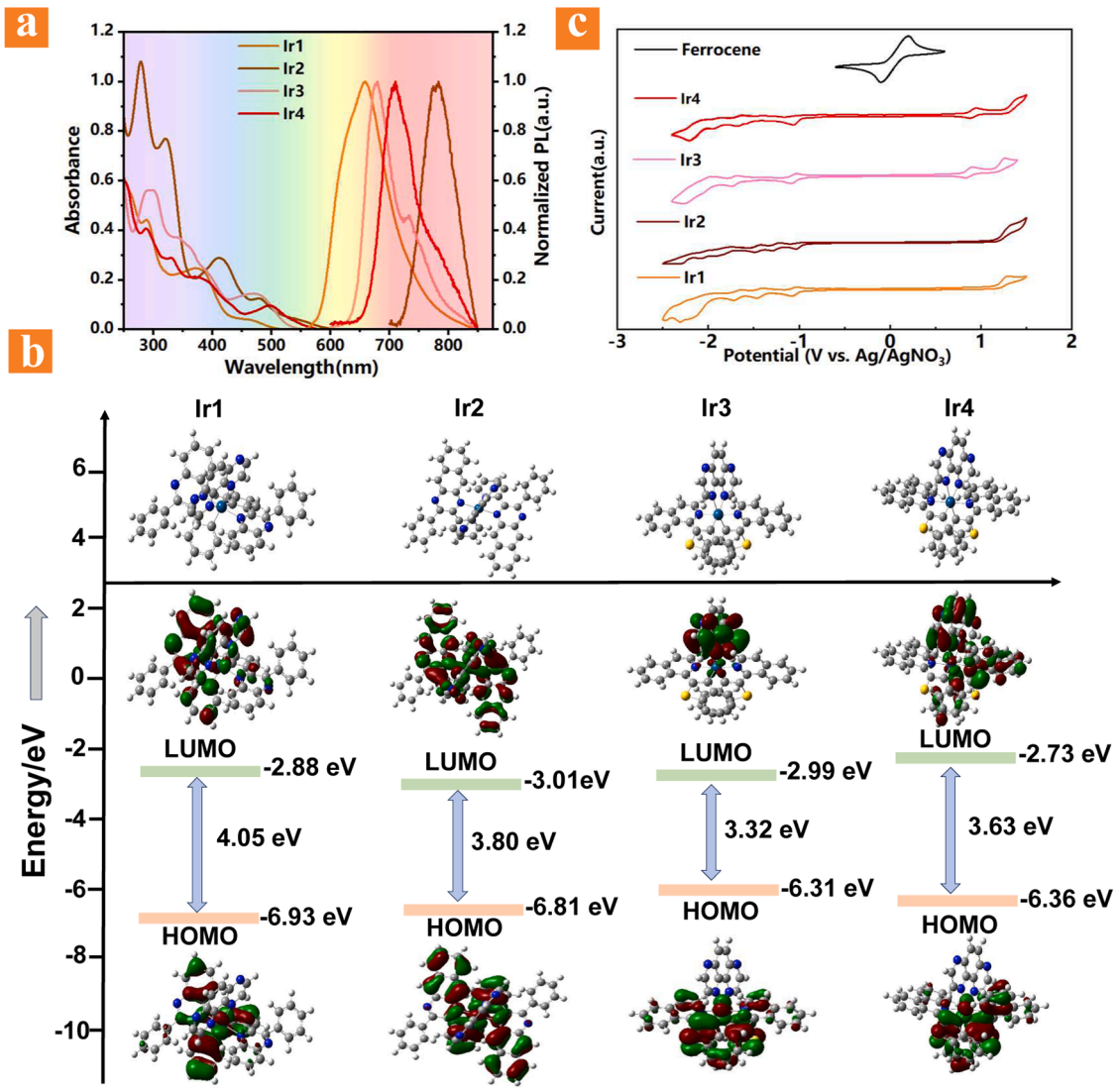

Fig. 1. (a) Absorbance spectra and normalized emission spectra of Ir1–Ir4 in acetonitrile. (b) Calculated energy levels, HOMO-LUMO gaps and frontier molecular orbital distributions of Ir1–Ir4. (c) Cyclic voltammetry curves of ferrocene and complexes Ir1–Ir4 in acetonitrile.

Table 1
Photophysical data for Ir1–Ir4 in acetonitrile at 298 K.

Complex	λ_{abs}/nm(ε/10^4 $M^{-1}cm^{-1}$)	λ_{max}(em)/nm	τ/ns	Φ
Ir1	290(3.68), 372(2.07), 459(0.34)	659	366	2.05
Ir2	279(6.36), 323(4.51), 417(1.67), 483 (0.72)	783	481	0.12
Ir3	295(3.51), 349(2.25), 475(0.90)	679	417	1.08
Ir4	290(4.04), 332(2.28), 385(2.04), 493 (0.93)	712	414	0.12

evidenced by their sustained radiative lifetimes (366–481 μs) observed in air-equilibrated solutions (Table 1). The broad and structureless photoluminescence bands of Ir1, Ir2 and Ir4 have an obvious MLCT feature, evidenced by the positive solvatochromism (Table S1), while Ir3 manifests comparable luminescence signatures in PL spectra, featuring a spectral shoulder at 730 nm indicative of hybridized triplet charge-transfer states. The time-the dependent density functional theory (TD-DFT) calculations further indicates that the emission dominantly results from a mixture of ^{3}MLCT and ^{3}ILCT (Fig. 1b, Tables S2 and S3). It can be observed that the Ir2 with Dbq and Ir4 with Byp as the C^N ligand shows a lower-energy emission than Ir1 with Dpq and Ir3 with Bys as the C^N ligands, respectively, arising from extended π-conjugation within their respective ligand frameworks. Notably, the calculations confirmed the frontier orbital energetics display distinct modulation patterns: Ir2 exhibits a significantly elevated highest occupied molecular orbital (HOMO) energy level and a substantially lowered lowest unoccupied molecular orbital (LUMO) energy level relative to Ir1. In contrast, Ir4 shows a pronounced HOMO shift compared to Ir3, while its LUMO energy level remains virtually identical, suggesting ligand-specific orbital control in these photosensitizers.

The redox profiles of complexes Ir1–Ir4 versus the Ag/$AgNO_3$ reference electrode were acquired via cyclic voltammetry (CV), with corresponding electrochemical data compiled in Table S5. Distinct quasi-reversible redox transitions are observed for Ir1 and Ir2, whereas Ir3 and Ir4 exhibit well-defined reversible processes (Fig. 1c). The onset oxidation potentials (E_{ox}^{onset}) are measured as 1.29, 1.50, 0.89, and 0.92 V for Ir1, Ir2, Ir3, and Ir4, respectively. Applying the empirical relationship E_{HOMO} (eV) = −(E_{ox}^{onset} vs Fc/Fc^+ + 4.8), the calculated HOMO energy levels are −6.09, −6.30, −5.69, and −5.72 eV for Ir1–Ir4, respectively. The previous studies with analogues reveal that iridium complexes containing the same cyclometalating ligands as Ir3 or Ir4

generally exhibit lower oxidation potentials and significantly elevated HOMO energy levels compared to those with ligands analogous to Ir1 or Ir2, which aligns consistently with the cyclic voltammetry results [46–49]. During cathodic polarization scans, quasi-reversible reductive transitions are observed for these iridium(III) complexes. The onset reduction potentials (E_{red}^{onset}) are determined as −1.08, −1.03, −1.09, and −1.06 V for Ir1–Ir4, respectively, suggesting comparable photoreductive capabilities. Utilizing these E_{red}^{onset} values, the LUMO energy levels (E_{LUMO}) are derived via the empirical relation E_{LUMO} (eV) = −(E_{red}^{onset} vs Fc/Fc^+ + 4.8) yielding values of −3.72, −3.77, −3.71, and −3.74 eV for Ir1–Ir4. From these redox parameters, the electrochemical band gaps (E_g^{cv}) are computed as 2.37, 2.53, 1.98, and 1.98 eV for Ir1–Ir4, respectively. The distribution of LUMOs revealed that the ancillary ligand TAP predominantly governs the LUMOs, while the four cyclometalating ligands exhibit varying degrees of contribution to the LUMOs, resulting in energy-level slight fluctuations of the LUMOs and thereby enabling precise modulation of the energy gaps in these iridium complexes (Table S4). Frontier molecular orbital analyses reveal that the HOMO electron density in iridium(III) complexes Ir1–Ir4 is predominantly localized on the metal center and cyclometalating C^N ligand framework, with calculated HOMO/LUMO energy levels of −6.93/−2.88 eV (Ir1), −6.81/−3.01 eV (Ir2), −6.31/−2.99 eV (Ir3), and −6.36/−2.73 eV (Ir4), respectively. While discrepancies in HOMO/LUMO energy levels and electrochemical bandgaps between experimental (cyclic voltammetry) and theoretical (TD-DFT) approaches were observed for complexes Ir1–Ir4—primarily arising from solvation effects, electronic state disparities, and computational approximations—the strategic design of cyclometalating ligands effectively modulated the frontier orbital energetics. Notably, these findings establish that the molecular architecture of the coordinating ligands exerts deterministic control over the electronic structure of iridium(III) coordination systems.

3.3. Evaluation of ROS generation in aqueous media and proposed mechanism of PDT

The structural stability of photosensitizers under prolonged light irradiation is a critical evaluation criterion for their clinical application. Continuous irradiation tests were conducted on acetonitrile solutions of Ir1–Ir4 using a xenon lamp (400–800 nm, 100 mW/cm^2) for 6 min, with real-time monitoring through UV–vis absorption spectroscopy (Fig. S1). All complexes exhibited minimal photodegradation, indicating these iridium(III) complexes possess exceptional photochemical stability within the therapeutic wavelength range of PDT. This remarkable stability ensures reliable maintenance of their photosensitizing functionality during extended light exposure in clinical PDT applications, significantly enhancing their potential for practical implementation in cancer treatment protocols. To systematically evaluate the ROS generation performance of Ir1–Ir4 in solution, a dual detection system was employed for quantitative analysis of their photosensitizing capabilities. As illustrated in Figs. 2a and S2, the DCFH probe assays revealed that Ir1–Ir4 exhibited substantial ROS generation capabilities under both normoxic and hypoxic conditions, outperforming the reference complex Ir-TAP by a significant margin. Notably, Ir4 demonstrated the highest ROS generation efficiency under normoxic conditions (Fig. 2a), whereas Ir3 emerged as the most potent $^1O_2$ generator under hypoxic conditions mimicking the tumor microenvironment (Figs. 2b and S2). This oxygen-dependent divergence in ROS production profiles suggests that Ir1–Ir4 may engage distinct photosensitization mechanisms to generate heterogeneous ROS, potentially enabling adaptive therapeutic responses to varying oxygen tensions in biological systems.

To precisely identify the ROS subtype, a specialized ABDA (9,10-anthracenediyl-bis(methylene)dimalonic acid) trapping system was employed to quantify $^1O_2$ generation through characteristic absorption decay at 380 nm. The reference system featured the classical Type II photosensitizer $[Ru(bpy)_3]^{2+}$ (bpy = 2,2′-bipyridine). In air-saturated acetonitrile solutions containing Ir1–Ir4, UV–vis spectral monitoring was performed under standardized experimental conditions. For quantum yield determination, photosensitizer concentrations were adjusted

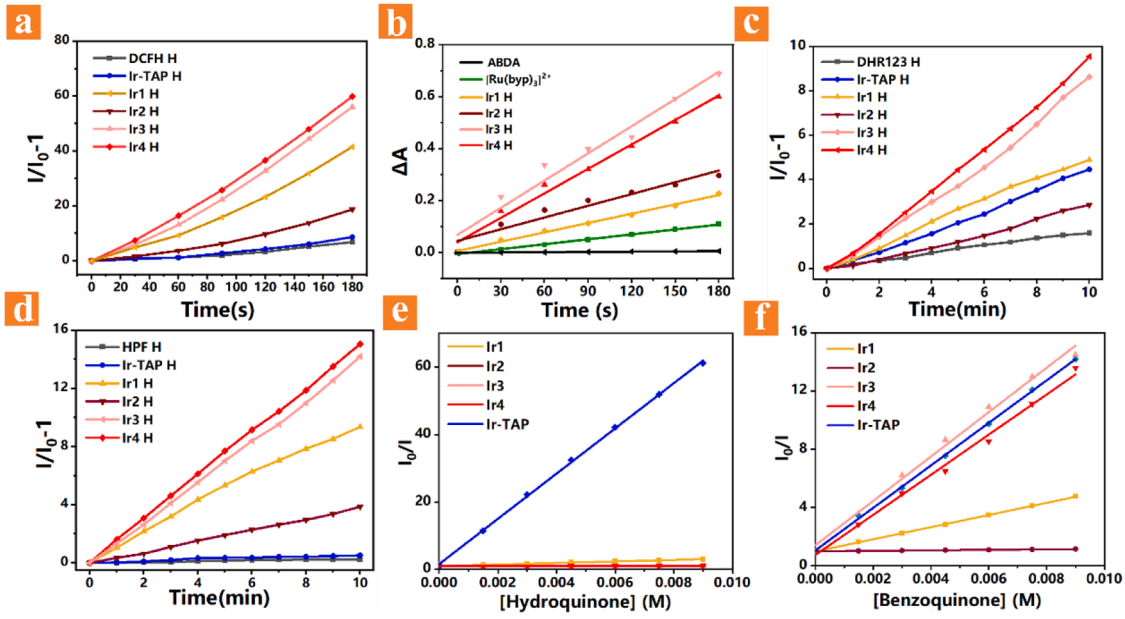

Fig. 2. (a) Emission intensity changes at 530 nm of DCFH in different iridium complexes-containing solutions during light irradiation under hypoxic conditions over 0–180 s. (b) The linear fitting curve of the absorbance variation at 400 nm for ABDA-containing solutions with different complexes under light irradiation over 0–180 s. (c) Emission intensity changes at 525 nm of DHR123 in different iridium complexes-containing solutions during light irradiation under hypoxic conditions over 0–10 min. (d) Emission intensity changes at 515 nm of HPF in different iridium complexes-containing solutions during light irradiation under hypoxic conditions over 0–10 min. H stands for hypoxic conditions. (e) Stern-Volmer plots obtained upon the addition of 1,4-hydroquinone to iridium complexes. (f) Stern-Volmer plots obtained upon the addition of 1, 4-benzoquinone to iridium complexes. Measurements made in acetonitrile.

to achieve an absorbance of 0.3 at 450 nm prior to 180-second irradiation with 450 nm light (100 mW/cm^2). Temporal absorbance changes were fitted to exponential decay curves for comparative analysis (Fig. S4). Remarkably, all iridium complexes demonstrated superior $^1O_2$ quantum yields compared to $[Ru(bpy)_3]^{2+}$, with Ir3 and Ir4 exhibiting ΦΔ values exceeding twice that of the reference compound, which could be attributed to the larger spin-orbit coupling constant of iridium compared to rutheniu. Parallel experiments under uniform photosensitizer concentration (10 μM) revealed significantly enhanced $^1O_2$ production by Ir2-Ir4 relative to the ruthenium benchmark. The comparatively lower photosensitization efficiency of Ir1 likely originates from its significantly lower molar extinction coefficient at 450 nm, highlighting structure-property correlations in these photodynamic agents.

To further validate the superoxide anion ($O_2^{\cdot-}$) and hydroxyl radical (·OH) generation capabilities of complexes Ir1–Ir4, targeted fluorescence assays were performed using dihydrorhodamine 123 (DHR123) and hydroxyphenyl fluorescein (HPF) as selective molecular probes. As demonstrated in Figs. 2c and S5, all iridium complexes exhibited time-dependent fluorescence enhancement in DHR123-containing solutions under broadband irradiation (400–800 nm), regardless of oxygen tension. Notably, Ir4 displayed the most pronounced fluorescence intensity increase under both normoxic and hypoxic conditions, indicating its superior $O_2^{\cdot-}$ generation capacity. Complementary experiments under tumor-mimetic hypoxia (1 % O_2) using HPF probes (Fig. 2d) revealed significant irradiation-dependent fluorescence amplification for all complexes, confirming effective ·OH production. The ·OH generation efficacy followed the hierarchy: Ir4 > Ir3 > Ir1 > Ir2. Control groups without photosensitizers or containing reference complex Ir-TAP showed negligible fluorescence changes, excluding nonspecific background signals. The differential ROS generation profiles observed across oxygen gradients and detection systems suggest oxygen tension-dependent activation mechanisms in these iridium-based photosensitizers. Comprehensive evaluation integrating total ROS yield under hypoxia, Type I ROS generation efficiency, excitation wavelength compatibility, and luminescence quantum efficiency identified Ir4 could be the optimal candidate for in vivo applications targeting hypoxic tumors (Table S5).

These iridium(III) complexes demonstrated predominant Type I photodynamic pathways in ROS generation assays. To elucidate the underlying photochemical mechanisms, investigations of their photo-oxidation and photo-reduction behaviors were conducted via steady-state photoluminescence quenching studies employing hydroquinone/benzoquinone (HQ/BQ) redox mediators in acetonitrile matrices. In photo-oxidation studies with HQ (Fig. 2e), significant luminescence quenching was observed for reference complex Ir-TAP with increasing HQ concentration. Notably, Ir1 exhibited only marginal emission attenuation, while Ir2-Ir4 maintained stable luminescence profiles, indicating limited electron-accepting capability from HQ under irradiation. This suggests that only Ir1 possesses moderate photoactivated oxidizability through interfacial electron transfer from HQ, whereas Ir2-Ir4 lack substantial oxidative photochemical activity. Conversely, photo-reduction experiments with BQ revealed distinct phosphorescence quenching patterns (Fig. 2f). Ir1, Ir3, and Ir4 displayed pronounced emission attenuation with BQ addition, demonstrating strong photoactivated reducibility through electron injection to BQ. The minimal luminescence variation observed for Ir2 likely stems from its inherently low photoluminescence quantum yield, which compromises detectable emission signal changes during redox processes. The bimolecular quenching rate constants (compiled in Table S6) approach the diffusion-controlled regime, signifying marked efficiency in reductive quenching dynamics that align with the oxidation potentials of these complexes. These results indicated that these iridium complexes enable efficient Type I photodynamic activity upon light. Unlike complex Ir-TAP, where the Type I mechanism originates from photoinduced electron acquisition, the Type I pathway in these complexes is predominantly initiated by photoinduced electron donation, which may be rationalized by the dominant contribution of metal-to-ligand charge transfer (MLCT) excited states in the complexes[50].The proposed mechanism of PDT for these complexes maybe that synergistic interplay between electron-rich cyclometalating ligands and electron-deficient ancillary ligands enables these complexes to operate in a pump-like mechanism under photoexcitation, efficiently shuttling electrons to proximal electron-accepting substrates while replenishing electrons from strongly reducing donor species (Fig. S6).

3.4. PDT in vitro

Building upon the promising photodynamic properties of iridium(III) complexes Ir1–Ir4, which demonstrated exceptional ROS generation capability in oxygen-deprived aqueous solutions under light irradiation, we subsequently investigated their intracellular PDT efficacy. The ROS production in live cells was quantitatively monitored through application of 2′,7′-dichlorodihydrofluorescein diacetate (DCFH-DA) functioning as a fluorogenic redox-sensitive indicator. This cell-permeable indicator undergoes enzymatic deacetylation to form DCFH, which subsequently reacts with multiple ROS subtypes to yield the fluorescent product 2′,7′-dichlorofluorescein, emitting characteristic green fluorescence (λ_{ex} = 488 nm, λ_{em} = 525 nm) upon photoexcitation. Figs. 3a and S7 reveal that all of four iridium complexes maintained remarkable ROS generation efficiency under hypoxic conditions (1 % O_2), consistent with their solution-phase performance. Notably, bright-field microscopy combined with long-pass filter imaging (>650 nm) demonstrated effective cellular internalization of these Ir(III) photosensitizers, while their intrinsic luminescence in the near-infrared window (650–750 nm) provided real-time tracking capability - a critical advantage for potential in vivo theranostic applications. To rigorously validate the photodynamic mechanism, two critical control experiments were implemented (Fig. 3a). The first control group (left panel) omitted the photosensitizer Ir4 while maintaining DCFH-DA incubation and light irradiation, showing minimal fluorescence signal. The second control (middle panel) retained both Ir4 and DCFH-DA but excluded light activation, demonstrating comparable basal fluorescence levels to the photosensitizer-free control. These orthogonal controls conclusively establish that the observed ROS elevation requires both photosensitizer presence and light activation. Notably, the maintenance of significant ROS generation under pathologically relevant hypoxic conditions (1 % O_2) suggests that these iridium(III) complexes overcome the critical oxygen dependency limitation of conventional PDT agents. This hypoxia-tolerant photodynamic activity positions Ir1–Ir4 as particularly promising candidates for treating solid tumors with characteristically hypoxic microenvironments. Furthermore, to differentiate the ROS subtypes generated during photodynamic activation, we conducted parallel experiments using hydroxyphenyl fluorescein (HPF), a selective probe for ·OH. As shown in Fig. 3b, distinct fluorescence signals within the 490–540 nm emission bandpass were detected across all photosensitizer-treated groups following light irradiation. Notably, while the fluorescence intensity measured by HPF was a slight lower than that quantified using DCFH-DA, this differential response aligns with the distinct chemical reactivities of these probes: DCFH-DA detects broad-spectrum ROS whereas HPF specifically responds to ·OH. This observed hierarchy in signal magnitude (DCFH-DA > HPF) provides mechanistic evidence that the Ir(III) complexes predominantly generate ·OH through Type I photochemical pathways under hypoxic conditions. The concordance between cellular and solution-phase analyses confirms that these metallophotosensitizers maintain their hypoxia-tolerant Type I photodynamic activity across heterogeneous biological environments.

To systematically investigate the hypoxia-tolerant PDT performance of these iridium complexes, we employed a dual-staining assay utilizing fluorescein diacetate (FDA) and propidium iodide (PI). FDA, a non-fluorescent esterase substrate, is enzymatically hydrolyzed to green-fluorescent fluorescein exclusively in viable cells with active

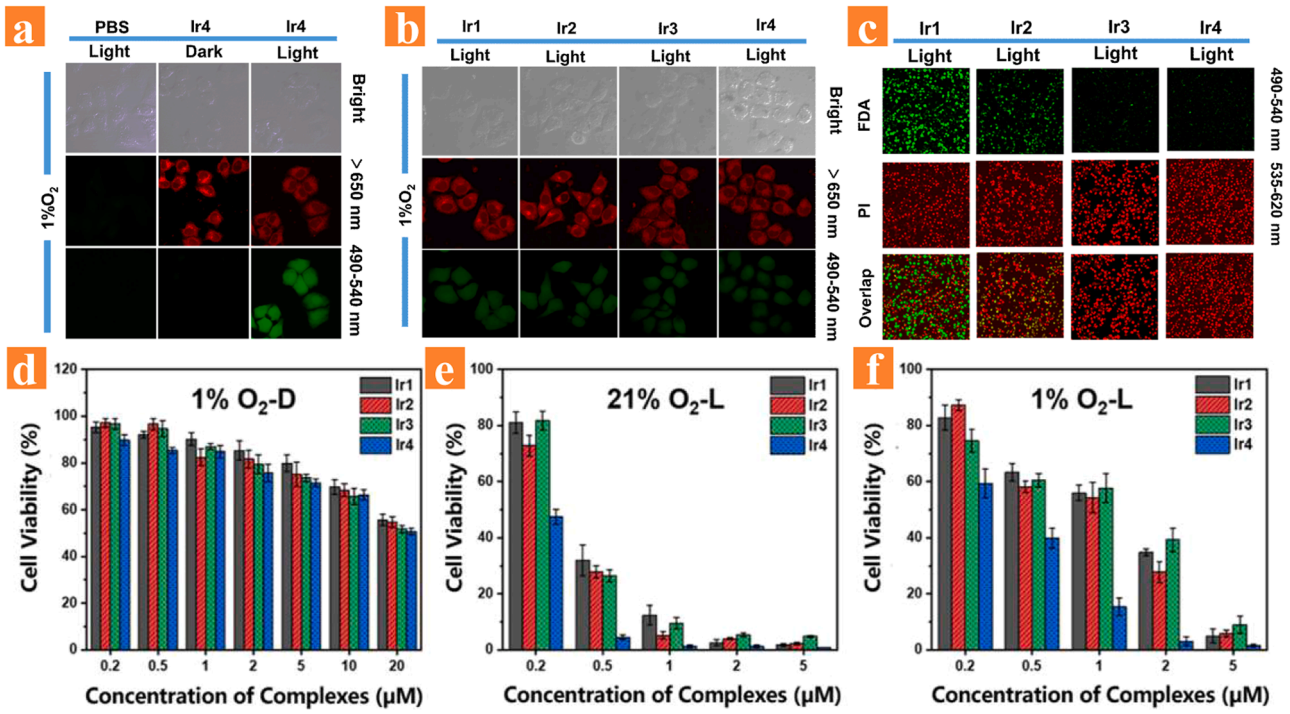

Fig. 3. (a) Representative confocal microscopy images of DCFH-stained cells with different treatments under hypoxic conditions. The light groups were irradiated with white light (400–800 nm, 25 mW/cm^2, 3 min). (b) Confocal microscopy images of complexes-loaded cells incubated with HPF after irradiation (400–800 nm, 25 mW/cm^2, 8 min) under hypoxic conditions. (c) Confocal microscopy images of complexes-loaded cells incubated with FDA and PI after irradiation under hypoxic conditions. (d) Dose-dependent viability of HeLa cells treated with complexes using CCK-8 assay in the dark (D). (e) Dose-dependent viability of HeLa cells treated with complexes using CCK-8 assay upon light (L) irradiation (400–800 nm, 25 mW/cm^2, 13 min) under normoxic conditions. (f) Dose-dependent viability of HeLa cells treated with complexes using CCK-8 assay upon light irradiation under hypoxic conditions.

intracellular esterases, whereas PI selectively permeates compromised cell membranes of nonviable cells, binding to nuclear DNA to emit red fluorescence. As shown in Fig. 3c, under hypoxic conditions with light irradiation, cells treated with Ir1 exhibited attenuated green fluorescence (indicating partial esterase activity) accompanied by prominent PI nuclear staining, suggesting limited PDT efficacy. In stark contrast, Ir2-Ir4-treated groups demonstrated complete loss of FDA-derived fluorescence with uniformly intensified PI signals, revealing near-total cell death and confirming their robust hypoxia-resistant PDT performance, further supporting their translational potential for treating hypoxic tumors.

To quantitatively assess the therapeutic potential of Ir1–Ir4 under pathologically relevant conditions, we performed CCK-8 cytotoxicity assays in hypoxic (1 % O_2) and normoxic environments. As summarized in Fig. 3d–f, all four complexes exhibited minimal dark toxicity (<15 % cell death at 10 μM) during co-incubation with HeLa cells without light activation, confirming their biocompatibility for potential clinical translation. Under white light irradiation (20 J/cm^2) under normoxic conditions, a dramatic reduction in cell viability was observed. The measured IC50 values fell below 1 μM, demonstrating a photodynamic potency that surpasses most clinically investigated photosensitizers. Remarkably, even under oxygen-deprived conditions, Ir1–Ir4 maintained substantial photocytotoxicity, particularly Ir4 demonstrating 48.3 % cell death at 1 μM. The calculated phototoxicity indices (PI = IC_{50} dark/IC_{50} light) under hypoxia consistently exceeded 9.0 across all complexes (Table S7), quantitatively validating their hypoxia-tolerant PDT efficacy. This oxygen-independent antitumor performance mechanistically aligns with our earlier spectroscopic evidence of Type I-dominated ROS generation. The combined pharmacological and mechanistic data position these Ir(III) complexes as first-in-class metallophotosensitizers capable of overcoming the intrinsic hypoxia limitations of conventional PDT, particularly promising for treating deeply seated or poorly vascularized tumors.

3.5. PDT in vivo

Encouraged by its outstanding performance in cellular experiments, the in vivo PDT of Ir4 is then investigated by employing the xenograft Hela-subcutaneous tumor-bearing mouse model. All the mice experiments were carried out in accordance with the relevant laws and the guidelines of Institutional Animal Care and Use Committee. Firstly, the mouse was anesthetized by isoflurane for the in vivo luminescence imaging after intratumoral injection of Ir4 (1 mM, 25 mL/50 mm^3 tumor) for 4 h (Fig. 4a). The intense luminescence at the tumor site can be observed intuitively, which indicates that Ir4 is not metabolized quickly and in favor of potential tumor imaging and subsequent PDT assessment. The tumor-bearing mice were then randomly divided into three groups, with five mice in each group: the control group, the dark group and the PDT group. The mice treated with light or Ir4 alone served as the control group (PBS + light) and the dark group (Ir4 + Dark), respectively. For the mice in the PDT group (defined as Ir4 + light), a solution of Ir4 (1 mM, 25 mL/50 mm^3 tumor) was injected intratumorally into the tumor-bearing mice and tumor regions were irradiated by a xenon lamp (250 mW/cm^2, 10 min) at 0.5 h post injection. As for the other two groups, tumor-bearing mice were treated with the same volume of PBS and light, or the same solution of Ir4 only. During the in vivo PDT experiments, Longitudinal tumor volumetry (calculated as [length × width^2]/2) and somatic mass indices were systematically quantified at defined temporal intervals throughout the therapeutic regimen. As shown in Fig. 4b, the neoplasm volumes hardly increased for the mice subjected to Ir4 and light, manifesting the tumors growth of mice in the PDT group were remarkably inhibited, while tumors in the mice treated with PBS and irradiation or those administered with Ir4 only grew rapidly and exhibited barely tumor-size restraint, proving that Ir4 or the used light had no antitumor efficacy themselves. Meanwhile, the body weight-growth curves about all treated mice showed a slight elevation and no apparent changes in each group throughout the entire treatment period

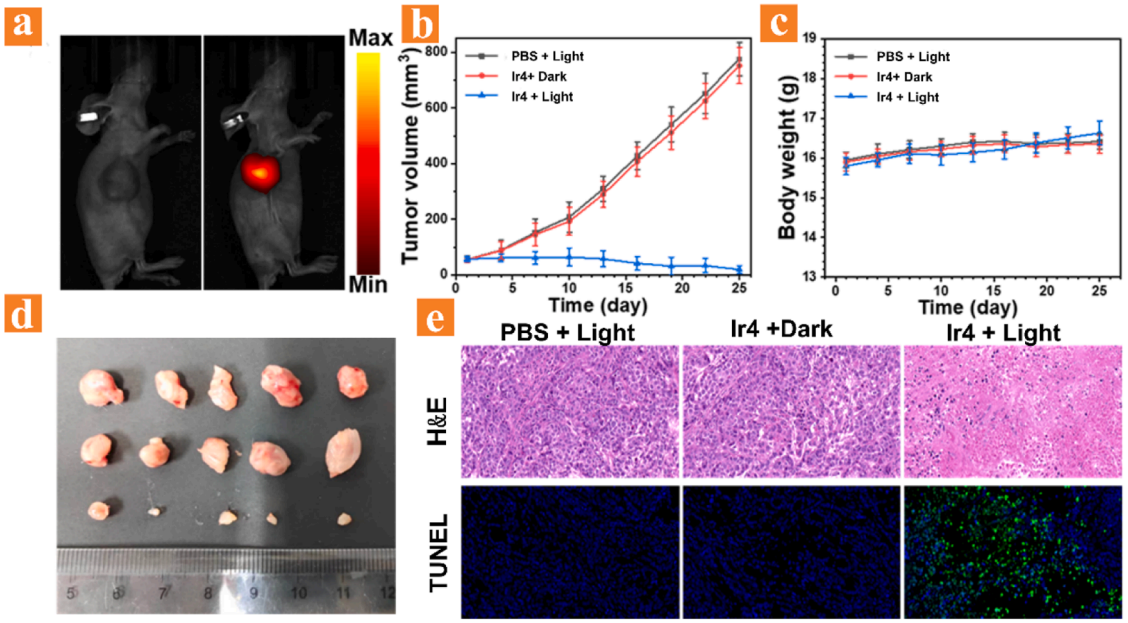

Fig. 4. (a) In vivo photoluminescence signal images 24 h after Ir4 (1 mM, 25 mL/50 mm^3) injection into the tumor. (b) Tumor growth curve of mice with different treatments. (c) body weight gain curve of mice with different treatments. (d) Representative images of tumors collected from mice with different treatments. (e) H&E and TUNEL staining images of tumors treated with PBS or Ir4 under different conditions. The tumors were irradiated with white light (400–800 nm, 250 mW/cm^2, 10 min).

(Fig. 4c). These results revealed that Ir4 possessed an effective PDT potency and a little dark toxicity to these mice preliminarily. Furthermore, the main organs and tumors were collected for histological analysis performed by hematoxylin eosin (H&E) after the mice were sacrificed on day 25 (Fig. 4d). Results showed that no discernible structural alterations in tumor lesions or vital organs (cardiac, hepatic, splenic, pulmonary, and renal tissues) within tissue sections derived from PBS- or Ir4-treated cohorts, as shown in Fig. S8. On the contrary, the tumor sections of the PDT group were sparsely aligned with large necrosis (Fig. 4e). Incidentally, the terminal deoxynucleotidyl transferase dUTP nick end labeling (TUNEL) assays were performed on tumor xenografts to delineate the antitumor mechanism of Ir4 in vivo. As depicted in Fig. 4e, the fluorescence TUNEL staining of tumors from mice subjected to various treatments clearly illustrated that a significantly highest percentage of TUNEL-positive apoptotic cells compared to the other two groups. These results verified that Ir4 indeed has negligible cumulative effect or adverse biological effects to the living mice, and effective PDT potency under light irradiation.

4. Conclusion

In conclusion, to circumvent the limitations imposed by tumor hypoxia on photosensitizer performance and enhance therapeutic efficacy under oxygen-deprived conditions, this study adopts a molecular engineering approach. Four cyclometalating ligands with distinct conjugation architectures (Dpq, Dbq, Bys, Byp) were judiciously paired with the electron-deficient ancillary ligand TAP to construct near-infrared emissive ($\lambda > 650$ nm) iridium(III) complexes Ir1–Ir4. Compared to the benchmark complex Ir-TAP, these derivatives exhibit significantly enhanced photodynamic activity under visible-light irradiation. Crucially, Ir3 and Ir4 - featuring lower oxidation potentials—demonstrate hypoxia-tolerant Type I photodynamic behavior, efficiently generating superoxide radicals and hydroxyl radicals to trigger apoptotic pathways. In vivo studies confirm the superior antitumor efficacy of Ir4 when activated by white light. Importantly, this work establishes a rational design strategy combining strong electron-donating cyclometalating ligands with electron-withdrawing ancillary ligands to engineer Type I complex photosensitizers with photoactivated electron-pumping mechanisms.

CRediT authorship contribution statement

Zejing Chen: Writing – review & editing, Writing – original draft, Resources, Methodology, Investigation, Formal analysis, Data curation, Conceptualization. **Qingchao Tu:** Writing – original draft, Methodology, Formal analysis, Data curation. **Peiling Dai:** Methodology, Investigation. **Yunjian Xu:** Methodology, Data curation. **Wenyuan Xu:** Methodology. **Jingjing Xue:** Validation. **Haiyong Ao:** Methodology. **Xiaoming Hu:** Writing – review & editing, Supervision, Methodology, Funding acquisition, Conceptualization. **Wei Jiang:** Writing – original draft, Investigation, Formal analysis, Data curation. **Shujuan Liu:** Supervision. **Qiang Zhao:** Writing – review & editing, Supervision.

Declaration of competing interest

The authors declare that they have no known competing financial interests or personal relationships that could have appeared to influence the work reported in this paper.

Acknowledgments

This work was supported by the National Natural Science Foundation of China (22001069, 22465015 and 82302257), Natural Science Foundation of Jiangxi Province (20224BAB204007, 20242BAB22007, 20232BAB203049 and 20243BCE51136) and the open research fund of Key Laboratory for Organic Electronics and Information Displays.

Supplementary materials

Supplementary material associated with this article can be found, in the online version, at doi:10.1016/j.jorganchem.2025.123750.

Data availability

Data will be made available on request.

References

[1] P. Agostinis, K. Berg, K.A. Cengel, T.H. Foster, A.W. Girotti, S.O. Gollnick, S. M. Hahn, M.R. Hamblin, A. Juzeniene, D. Kessel, M. Korbelik, J. Moan, P. Mroz, D. Nowis, J. Piette, B.C. Wilson, J. Golab, Photodynamic therapy of cancer: an update, CA Cancer J. Clin. 61 (4) (2011) 250–281.

[2] D. Dolmans, D. Fukumura, R.K. Jain, Photodynamic therapy for cancer, Nat. Rev. Cancer 3 (5) (2003) 380–387.

[3] W.R. Wilson, M.P. Hay, Targeting hypoxia in cancer therapy, Nat. Rev. Cancer 11 (6) (2011) 393–410.

[4] W.P. Fan, P. Huang, X.Y. Chen, Overcoming the Achilles' heel of photodynamic therapy, Chem. Soc. Rev. 45 (23) (2016) 6488–6519.

[5] Y.B. Zhang, J.Q. Xing, J. Jiang, M.L. Liao, G.J. Pan, Y.F. Wang, Hypoxia-responsive nanoparticles for fluorescence diagnosis and therapy of cancer, Theranostics 15 (4) (2025) 1353–1375.

[6] X.S. Li, N. Kwon, T. Guo, Z. Liu, J. Yoon, Innovative strategies for hypoxic-tumor photodynamic therapy, Angew. Chem. Int. Ed. 57 (36) (2018) 11522–11531.

[7] T. Xiong, Y.C. Chen, M.L. Li, X.Q. Chen, X.J. Peng, Recent progress of molecular design in organic type I photosensitizers, Small (2025), https://doi.org/10.1002/smll.202501911.

[8] N. Kotagiri, G.P. Sudlow, W.J. Akers, S. Achilefu, Breaking the depth dependency of phototherapy with Cerenkov radiation and low-radiance-responsive nanophotosensitizers, Nat. Nanotechnol. 10 (4) (2015) 370–379.

[9] M. Zhang, Z.W. Cui, R.X. Song, B. Lv, Z.M. Tang, X.F. Meng, X.Y. Chen, X.P. Zheng, J.W. Zhang, Z.W. Yao, W.B. Bu, $SnWO_4$-based nanohybrids with full energy transfer for largely enhanced photodynamic therapy and radiotherapy, Biomaterials 155 (2018) 135–144.

[10] H.B. Chen, Z.J. Gu, H.W. An, C.Y. Chen, J. Chen, R. Cui, S.Q. Chen, W.H. Chen, X. S. Chen, X.Y. Chen, Z. Chen, B.Q. Ding, Q. Dong, Q. Fan, T. Fu, D.Y. Hou, Q. Jiang, H.T. Ke, X.Q. Jiang, G. Liu, S.P. Li, T.Y. Li, Z. Liu, G.J. Nie, M. Ovais, D.W. Pang, N. S. Qiu, Y.Q. Shen, H.Y. Tian, C. Wang, H. Wang, Z.Q. Wang, H.P. Xu, J.F. Xu, X. L. Yang, S. Zhu, X.C. Zheng, X.Z. Zhang, Y.B. Zhao, W.H. Tan, X. Zhang, Y.L. Zhao, Precise nanomedicine for intelligent therapy of cancer, Sci. China-Chem. 61 (12) (2018) 1503–1552.

[11] H.R. Hou, S.W. Wei, Y.T. Shao, Y.N. Wu, G.B. Hong, J. An, J.R. Tian, J.J. Du, F. L. Song, X.J. Peng, A 690-nm-excitable type I & II photosensitizer based on biotinylation of verteporfin for photodynamic therapy of deep-seated orthotopic breast tumors, Chin. Chem. Lett. 36 (6) (2025) 110315.

[12] E.F.F. Silva, C. Serpa, J.M. Dabrowski, C.J.P. Monteiro, S.J. Formosinho, G. Stochel, K. Urbanska, S. Simoes, M.M. Pereira, L.G. Arnaut, Mechanisms of singlet-oxygen and superoxide-ion generation by porphyrins and bacteriochlorins and their implications in photodynamic therapy, Chem. Eur. J. 16 (30) (2010) 9273–9286.

[13] E. Yang, J.R. Diers, Y.Y. Huang, M.R. Hamblin, J.S. Lindsey, D.F. Bocian, D. Holten, Molecular electronic tuning of photosensitizers to enhance photodynamic therapy: synthetic dicyanobacteriochlorins as a case study, Photochem. Photobiol. 89 (3) (2013) 605–618.

[14] S. Singh, A. Aggarwal, N. Bhupathiraju, G. Arianna, K. Tiwari, C.M. Drain, Glycosylated porphyrins, phthalocyanines, and other porphyrinoids for diagnostics and therapeutics, Chem. Rev. 115 (18) (2015) 10261–10306.

[15] Y. Pei, Y. Pan, Z. Zhang, J. Zhu, Y. Sun, Q. Zhang, D. Zhu, G. Li, M.R. Bryce, D. Wang, B.Z. Tang, Leveraging tumor microenvironment to boost synergistic photodynamic therapy, ferroptosis anti-tumor efficiency based on a functional iridium(III) complex, Adv. Sci. (Weinh.) 12 (14) (2025) e2413879.

[16] H. Chen, S. Liu, W. Wang, F. Long, Q. Li, D. Gan, X. Li, B. Li, X. Kong, D. Li, Y. Chang, Synergistic comprehensive activation methods for dual-modality PDT and hypoxia-triggered chemotherapy guided by NIR-II imaging beyond 1700 nm in deep tumors, Small (2025) e2500553.

[17] L.C.C. Lee, K.K.W. Lo, Luminescent and photofunctional transition metal complexes: from molecular design to diagnostic and therapeutic applications, J. Am. Chem. Soc. 144 (32) (2022) 14420–14440.

[18] P. Tao, Z. Lv, F.Q. Zhao, X.K. Zheng, H. Jiang, W.T. Li, Y.J. Deng, S.J. Liu, G.H. Xie, W.Y. Wong, Q. Zhao, One-pot synthesis of acetylacetonate-based isomeric phosphorescent cyclometalated iridium(III) complexes via random cyclometalation: a strategy for excited-State manipulation, Inorg. Chem. 62 (3) (2023) 1202–1209.

[19] J. Su, J. Wei, K.S. Ye, F.Y. Li, M.Z. Wang, Q.X. Li, A.H. Yuan, Q. Zhao, C. Shi, Tuning charge transfer properties in symmetric and asymmetric pyrrolo 3,2-b pyrrole derivatives with hybridized local and charge-transfer characteristics, Chem. Commun. 61 (29) (2025) 5475–5478.

[20] Z. Chen, J. Jiang, W. Zhao, X. Hu, M. Xie, F. Li, S. Liu, Q. Zhao, An aggregation-induced phosphorescent emission-active iridium(III) complex for fluoride anion imaging in living cells, J. Organomet. Chem. 932 (2021) 121644.

[21] S. Liu, Y. Pei, Y. Sun, Z. Wang, H. Chen, D. Zhu, M.R. Bryce, B.Z. Tang, Y. Chang, Three birds with one stone" nanoplatform: efficient near-infrared-triggered type-I AIE photosensitizer for mitochondria-targeted photodynamic therapy against hypoxic tumors, Aggregate 5 (4) (2024) e547.

[22] P. Tao, Z. Lv, X.K. Zheng, H. Jiang, S.J. Liu, H. Wang, W.Y. Wong, Q. Zhao, Isomer engineering of lepidine-based iridophosphors for far-red hypoxia imaging and photodynamic therapy, Inorg. Chem. 61 (44) (2022) 17703–17712.

[23] Z. Chen, X. Meng, M. Xie, Y. Shi, L. Zou, S. Guo, J. Jiang, S. Liu, Q. Zhao, A self-calibrating phosphorescent polymeric probe for measuring pH fluctuations in subcellular organelles and the zebrafish digestive tract, J. Mater. Chem. C 8 (7) (2020) 2265–2271.

[24] Z. Chen, X. Meng, L. Zou, M. Zhao, S. Liu, P. Tao, J. Jiang, Q. Zhao, A dual-emissive phosphorescent polymeric probe for exploring drug-induced liver injury via imaging of peroxynitrite elevation In vivo, ACS Appl. Mater. Interface. 12 (11) (2020) 12383–12394.

[25] A. Panwar, C.C. Malakar, A. Upadhyay, M. Roy, A red light-activable hetero-bimetallic complex as a dual-modality PDT tool for anticancer therapy, Dalton Trans. 54 (11) (2025) 4474–4483.

[26] C.E. Housecroft, E.C. Constable, Over the LEC rainbow: colour and stability tuning of cyclometallated iridium(III) complexes in light-emitting electrochemical cells, Coord. Chem. Rev. 350 (2017) 155–177.

[27] Z. Chen, K.Y. Zhang, X. Tong, Y. Liu, C. Hu, S. Liu, Q. Yu, Q. Zhao, W. Huang, Phosphorescent polymeric thermometers for In vitro and In vivo temperature sensing with minimized background interference, Adv. Funct. Mater. 26 (24) (2016) 4386–4396.

[28] Z. Chen, P. Yan, L. Zou, M. Zhao, J. Jiang, S. Liu, K.Y. Zhang, W. Huang, Q. Zhao, Using ultrafast responsive phosphorescent nanoprobe to visualize elevated peroxynitrite In vitro and In vivo via ratiometric and time-resolved photoluminescence imaging, Adv. Healthc. Mater. 7 (16) (2018) e1800309.

[29] R. Liu, G. Zhang, M.Y. He, X.L. Li, J. Tang, Y.L. Liu, S. Guo, Solution-processed red organic light-emitting diodes based on phosphorescent iridium(III) complex with isoquinoline derivative as the main ligand, J. Organomet. Chem. 1031 (2025) 123594.

[30] P. Tao, X. Lü, G. Zhou, W.-Y. Wong, Asymmetric tris-heteroleptic cyclometalated phosphorescent iridium(III) complexes: an emerging class of metallophosphors, Acc. Mater. Res. 3 (8) (2022) 830–842.

[31] P.L. Dai, C.X. Luo, Z.Q. Xu, S.S. Sun, Y.Y. Tian, K.Y. Zhang, K.K.W. Lo, S.J. Liu, W. Huang, H. Wang, Q. Zhao, Phosphorescent iridium(III) phenanthrolinedione complexes as lifetime-responsive bioorthogonal probes for wash-free time-resolved bioimaging of cellular labeling, Angew. Chem.Int. Ed. (2025), https://doi.org/10.1002/anie.202504230.

[32] Y.L. Zeng, L.Y. Liu, T.Z. Ma, Y. Liu, B. Liu, W. Liu, Q.H. Shen, C. Wu, Z.W. Mao, Iridium(III) photosensitizers induce simultaneous pyroptosis and ferroptosis for Multi-network synergistic tumor immunotherapy, Angew. Chem. Int. Ed. Engl. 63 (49) (2024) e202410803.

[33] Z. Zhang, Z. Wei, J. Guo, J. Lyu, B. Wang, G. Wang, C. Wang, L. Zhou, Z. Yuan, G. Xing, C. Wu, X. Zhang, Metallopolymer strategy to explore hypoxic active narrow-bandgap photosensitizers for effective cancer photodynamic therapy, Nat. Commun. 15 (1) (2024) 170.

[34] J.S. Nam, M.G. Kang, J. Kang, S.Y. Park, S.J.C. Lee, H.T. Kim, J.K. Seo, O.H. Kwon, M.H. Lim, H.W. Rhee, T.H. Kwon, Endoplasmic reticulum-localized iridium(III) complexes as efficient photodynamic therapy agents via protein modifications, J. Am. Chem. Soc. 138 (34) (2016) 10968–10977.

[35] V. Novohradsky, A. Rovira, C. Hally, A. Galindo, G. Vigueras, A. Gandioso, M. Svitelova, R. Bresolí-Obach, H. Kostrhunova, L. Markova, J. Kasparkova, S. Nonell, J. Ruiz, V. Brabec, V. Marchán, Towards novel photodynamic anticancer agents generating superoxide anion radicals: a cyclometalated IrIII complex conjugated to a far-red emitting coumarin, Angew. Chem. Int. Ed 58 (19) (2019) 6311–6315.

[36] H. Yuan, Z. Han, Y.C. Chen, F. Qi, H.B. Fang, Z.J. Guo, S.R. Zhang, W.J. He, Ferroptosis photoinduced by new cyclometalated iridium(III) complexes and its synergism with apoptosis in tumor cell inhibition, Angew. Chem. Int. Ed. 60 (15) (2021) 8174–8181.

[37] H.Y. Huang, S. Banerjee, K.Q. Qiu, P.Y. Zhang, O. Blacque, T. Malcomson, M. J. Paterson, G.J. Clarkson, M. Staniforth, V.G. Stavros, G. Gasser, H. Chao, P. J. Sadler, Targeted photoredox catalysis in cancer cells, Nat. Chem. 11 (11) (2019) 1041.

[38] J. Chen, Z.G. Sheng, H.Z. Zhang, C.H. Huang, M. Qin, B. Shao, J.Y. Mao, R. Q. Wang, J. Shao, B.Z. Zhu, Unusual iron-independent ferroptosis-like cell death induced by photoactivation of a typical iridium complex for hypoxia photodynamic therapy, ACS Appl. Mater. Interface. 17 (4) (2025) 5684–5694.

[39] C. You, L. Tian, J. Zhu, L. Wang, B.Z. Tang, D. Wang, The Midas touch by Iridium: a second near-infrared aggregation-induced emission-active metallo-agent for exceptional phototheranostics of breast cancer, J. Am. Chem. Soc. 147 (2) (2025) 2010–2020.

[40] M. Zheng, X. Lin, K. Xiong, X. Zhang, Y. Chen, L. Ji, H. Chao, A hetero-bimetallic Ru(II)-Ir(III) photosensitizer for effective cancer photodynamic therapy under hypoxia, Chem. Commun. (Camb.) 60 (20) (2024) 2776–2779.

[41] Y.H. Jiang, W. Zhu, Z.R. Xu, Z.J. Zhang, S. Tang, M.Z. Fan, Z.Z. Li, J.Y. Zhang, C. B. Yang, W.C. Law, K.T. Yong, D. Wang, G.X. Xu, B.Z. Tang, A mitochondrion-targeting two-photon photosensitizer with aggregation-induced emission characteristics for hypoxia-tolerant photodynamic therapy, Chem. Eng. J. 448 (15) (2022) 137604.

[42] J. Tong, X. Yang, X. Song, J. Liang, S. Huang, H. Mao, M. Akhtar, A. Liu, G.G. Shan, G. Li, AIE-active Ir(III) complexes as type-I dominant photosensitizers for efficient photodynamic therapy, Dalton Trans. 52 (4) (2023) 1105–1112.

[43] L. Wei, R. Kushwaha, A. Dao, Z. Fan, S. Banerjee, H. Huang, Axisymmetric bis-tridentate Ir(III) photoredox catalysts for anticancer phototherapy under hypoxia, Chem. Commun. (Camb.) 59 (21) (2023) 3083–3086.

[44] Z. Lv, H.J. Wei, Q. Li, X.L. Su, S.J. Liu, K.Y. Zhang, W. Lv, Q. Zhao, X.H. Li, W. Huang, Achieving efficient photodynamic therapy under both normoxia and hypoxia using cyclometalated Ru(II) photosensitizer through type I photochemical process, Chem. Sci. 9 (2) (2018) 502–512.

[45] R. Bevernaegie, B. Doix, E. Bastien, A. Diman, A. Decottignies, O. Feron, B. Elias, Exploring the phototoxicity of hypoxic active iridium(III)-based sensitizers in 3D tumor spheroids, J. Am. Chem. Soc. 141 (46) (2019) 18486–18491.

[46] M. Song, S.-J. Yun, K.-S. Nam, H. Liu, Y.-S. Gal, J.W. Lee, S.-H. Jin, J.Y. Lee, S. K. Kang, Y.I. Kim, Highly efficient solution-processed pure red phosphorescent

organic light-emitting diodes using iridium complexes based on 2,3-diphenylquinoxaline ligand, J. Organomet. Chem. 794 (2015) 197–205.
[47] G.Y. Chen, B.R. Chang, T.A. Shih, C.H. Lin, C.L. Lo, Y.Z. Chen, Y.X. Liu, Y.R. Li, J. T. Guo, C.W. Lu, Z.P. Yang, H.C. Su, Cationic Ir(III) emitters with near-infrared emission beyond 800 nm and their use in light-emitting electrochemical cells, Chem 25 (21) (2019) 5489–5497.
[48] M. Penconi, A.B. Kajjam, M.-C. Jung, M. Cazzaniga, C. Baldoli, D. Ceresoli, M. E. Thompson, A. Bossi, Advancing near-infrared phosphorescence with heteroleptic iridium complexes bearing a single emitting ligand: properties and organic light-emitting diode applications, Chem. Mater. 34 (2) (2022) 574–583.
[49] K.M. Kuznetsov, I.S. Kritchenkov, J.R. Shakirova, V.V. Gurzhiy, V.V. Pavlovskiy, V. V. Porsev, V.V. Sokolov, S.P. Tunik, Red-to-NIR iridium(III) emitters: synthesis, photophysical and computational study, the effects of cyclometallating and β-diketonate ligands, Eur. J. Inorg. Chem. 2021 (22) (2021) 2163–2170.
[50] X.L. Ma, L.H. Ma, S. Guo, Z.M. Zhang, T.B. Lu, Identifying the key photosensitizing factors over metal-organic frameworks for selective control of $^1O_2$ and O_2^- generation, Angew. Chem. Int. Ed. 64 (17) (2025), https://doi.org/10.1002/anie.202504230.